How to cite: *Angew. Chem. Int. Ed.* **2022,** *61,* e202209747
International Edition: doi.org/10.1002/anie.202209747
German Edition: doi.org/10.1002/ange.202209747

Micromotors Hot Paper

Self-Propelled Initiative Collision at Microelectrodes with Vertically Mobile Micromotors

Ziyi Guo[+], Yanfang Wu[+], Zhouzun Xie[+], Junming Shao, Jian Liu., Yin Yao, Joseph Wang, Yansong Shen, J. Justin Gooding,* and Kang Liang**

Abstract: Impact experiments enable single particle analysis for many applications. However, the effect of the trajectory of a particle to an electrode on impact signals still requires further exploration. Here, we investigate the particle impact measurements versus motion using micromotors with controllable vertical motion. With biocatalytic cascade reactions, the micromotor system utilizes buoyancy as the driving force, thus enabling more regulated interactions with the electrode. With the aid of numerical simulations, the dynamic interactions between the electrode and micromotors are categorized into four representative patterns: approaching, departing, approaching-and-departing, and departing-and-reapproaching, which correspond well with the experimentally observed impact signals. This study offers a possibility of exploring the dynamic interactions between the electrode and particles, shedding light on the design of new electrochemical sensors.

Introduction

The electrochemistry of particles impacting with an electrode is one of the single entity electrochemical methods showing potential for not only counting the particles but also investigating their heterogeneity.[1–4] The detected signal of single particles impacting with an electrode poised at a potential is influenced by several variables, including the intrinsic properties of the particles,[5] the interaction between particles and the electrode,[6] the signal generation mechanism,[7] and the applied potential.[8] In revealing the correspondence between different collision systems and the electrochemical signal variance, the recently reported stochastic collision approach revealed some early promises.[9,10] For example, one study from Long and co-workers successfully demonstrated high-resolution particle size measurements with mixed-sample systems.[6] After simulating and investigating the oxidative status of silver nanoparticles (NPs), the high adsorptive capacity of gold ultramicroelectrode ensured well-distinguishable size-dependent characteristic current traces.[6] Another study from He and co-workers integrated nanopores with carbon electrodes for nanocollisions in a quartz nanopipette.[7] This system was shown to be capable of differentiating metallic gold NPs and insulating polystyrene NPs with the shape of potential dip from open-circuit potential changes. In addition, Kwon and co-workers identified two types of collision current responses with silver NPs by switching the applied potential.[8] With a single type of NPs, both staircase and blip current signals were obtained in response to the hindered hydrazine diffusion and the oxidation of Ag NPs, respectively.

During the single NP collision, the motion trajectory for NP analytes approaching the electrode interface still remains unknown.[11] So far, the alteration of the particles and the applied potential lead to distinguishable signal variance, however, it remains an open challenge to clarify the correlation between the signal generation and the dynamics

[*] Dr. Z. Guo,[+] Dr. Z. Xie,[+] Dr. J. Liu., Prof. Y. Shen, Dr. K. Liang
School of Chemical Engineering, The University of New South Wales
Sydney, NSW 2052 (Australia)
E-mail: ys.shen@unsw.edu.au
kang.liang@unsw.edu.au

Dr. Z. Guo,[+] Dr. Y. Wu,[+] Dr. J. Liu., Prof. J. J. Gooding, Dr. K. Liang
Australian Centre for NanoMedicine, The University of New South Wales
Sydney, NSW 2052 (Australia)

Dr. Y. Wu,[+] Prof. J. J. Gooding
School of Chemistry, The University of New South Wales
Sydney, NSW 2052 (Australia)
E-mail: justin.gooding@unsw.edu.au

J. Shao
School of Materials Science and Engineering, Central South University
Changsha, 410083 (China)

Dr. Y. Yao
Electron Microscope Unit, The University of New South Wales
Sydney, NSW 2052 (Australia)

Prof. J. Wang
Department of Nanoengineering, University of California San Diego
La Jolla, CA 92093 (USA)

Dr. K. Liang
Graduate School of Biomedical Engineering, The University of New South Wales
Sydney, NSW 2052 (Australia)

[+] These authors contributed equally to this work.

of the collision system that might be able to be addressed with self-propelled nano/micromotors.

Artificial self-propelled nano/micromotors have been investigated in a multitude of contemporary technologies applied in various aspects.[12–14] Advances in strategies for manipulating the motion of micromachines,[15] controlling the shape and size of the motors,[16] and improving the biocompatibility of the materials used,[17] have created exciting opportunities for nano/micromotors in drug delivery,[18] biosensing[19] and environmental remediation.[20,21] The integration of impact experiments and self-propelled nano/micromotors takes the advantages of both the current responses at the single-particle level and the ability to precisely control the motion of these particles. In one study, Pumera and co-workers reported hydrogen peroxide (H_2O_2)-driven, bubble thrust micromotors, including Janus Ag micromotors and tubular Cu/Pt micromotors, for micro-collision experiments.[22] Their work highlighted the possibility of employing impact electrochemistry to evaluate the micromotor concentration and velocity based on the collision numbers and the magnitude of the current signals. However, without a strategy in controlling the micromotors, bubble thrust micromotors approached the electrodes from all directions, thus this system could not provide well-resolved information of the dynamics of individual particle collision on the electrode. In addition, the micromotor emitted free bubbles with similar dimensions as the micromotors, which could further confound the impact signals. Although the primary correlation between the micromotors and the collision signal has been discussed, employing self-propelled micromotors with precisely controlled motion is an attractive strategy for studying the effect of analyte trajectory on signal variation.

Here, we designed an enzymatic micromotor system for electrochemical collision experiment, which exhibited velocity controllable vertical motion in glucose solution using buoyancy as the driving force (Scheme 1). By encapsulating two enzymes, glucose oxidase (GOx) and catalase (CAT), in the porous metal–organic frameworks (MOFs), the MOF micromotor possesses a coupled biocatalytic reaction using glucose as the chemical fuel. After the addition of the micromotors to the working environment in the electrolyte, we obtained current spikes indicative of collision events. The number of spikes increased with the glucose concentration. Within a single collision experiment, we acquired four distinctive types of electrical current signals in the same collision setup, and the possible correlation between the signal variation and the trajectory of the micromotor was discussed. To verify the proposed signal generation mechanism, a particle-scale computational fluid dynamics (CFD) simulation was applied to reproduce the solid–liquid interaction, and the particles impact on the electrode was revealed with force analysis.[23] With a better understanding of the trajectory influence, it is possible to study the mobility of individual particles (and possibly self-swimming microbes/cells) with electrochemistry in the future. By virtue of the micromotors with controllable motion behaviors, this work offers a chance to explore and understand the real-time interaction between mobile particles and the electrode, which provides a new dimension to carry out collision

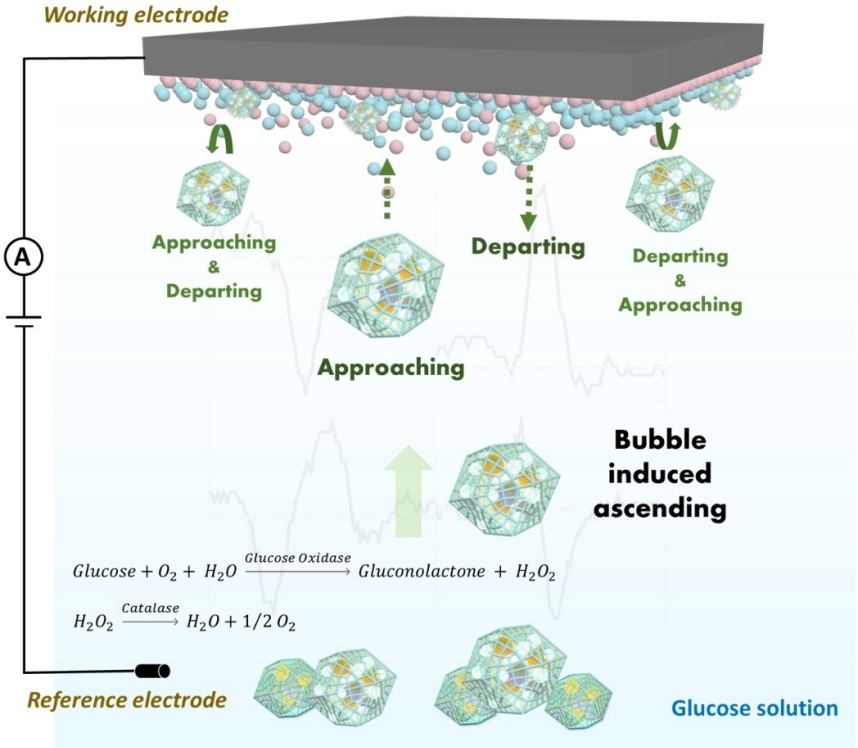

Scheme 1. Schematic illustration showing the collision mechanisms of the self-propelled micromotors. Micromotors are fabricated by co-encapsulating catalase and glucose oxidase into zeolitic imidazolate framework 8 (ZIF-8) particles.

experiments and sheds light on the development of electrochemical sensing.

Results and Discussion

Construction and Characterization of Self-Propelled Micromotor CAT-GOx@ZIF-8

Given the ease of engineering MOF microparticles with tunable pore size and surface chemistry,[24] MOFs are ideal materials for fabricating nano/micromotors.[25] Herein the MOF micromotor was synthesized in one pot as reported previously.[26,27] Briefly, the precursor solutions of 2-methylimidazole, CAT and GOx, and zinc nitrate, were mixed at room temperature. The particles formed by self-assembly were collected by centrifugation. The scanning electron microscopy (SEM) image and transmission electron microscopy (TEM) image of the obtained microparticles present a rhombic dodecahedron morphology of 800 nm in diameter (Figure 1a, b, Figure S1). To confirm the successful encapsulation of CAT and GOx in ZIF-8, these two enzymes were labeled with fluorescein isothiocyanate (FITC) and Alexa Fluor 647 (AF647), respectively. The resultant particles were imaged by a confocal laser scanning microscope (CLSM). The fluorescence distributions of green and red signals, indicating CAT and GOx, correlated well with that of the CAT-GOx@ZIF-8 (Figure 1c–e). The enzyme encapsulation efficiencies were measured with the fluorescence intensity of the synthetic supernatant and estimated to be 97 % and 89.3 % for CAT and GOx, respectively (Figure S2 and S3). The thickness distribution and uniform solid-state surface potential distribution of the CAT-GOx@ZIF-8 were measured with atomic force microscopy (AFM) (Figure 1f–h, Figure S4). The data indicated a uniformly distributed surface charge across the micromotor. Calibrated with highly ordered pyrolytic graphite (HOPG),[28] the surface work function (eV) of the micromotor was calculated to be 4.194 eV. The size distribution of the micromotors centered at 800 nm was measured with dynamic light scattering and presented in the histogram in Figure 1i.

The powder X-ray diffraction (PXRD) pattern of the CAT-GOx@ZIF-8 micromotor exhibited the characteristic peaks identical to standard ZIF-8, indicating the preservation of the ZIF-8 crystal structure (Figure S5). Due to the absence of carboxyl in ZIF-8 structures, the Fourier transform infrared spectroscopy (FTIR) patterns (Figure S6) at 1640 cm^{-1} (C=O stretching vibrations from amide I), 1533 cm^{-1} (C=N stretching vibrations from amide II) and 1098 cm^{-1} (C–O bond stretching vibration) confirmed the successful incorporation of the enzymes in the micromotor. The surface charge of the CAT-GOx@ZIF-8 micromotor was found to be negative in both Milli-Q water and electrolyte solution (2 mM NaCl, 0.1 mM $K_3Fe(CN)_6$ and 0.1 mM $K_4Fe(CN)_6$) (Figure S7 and S8). With the co-loading of CAT and GOx, the cascade reaction of glucose is given as below:

$$\text{Glucose} + O_2 + H_2O \rightarrow \text{Gluconolactone} + H_2O_2 \quad (1)$$

$$H_2O_2 \rightarrow H_2O + 1/2\,O_2 \quad (2)$$

As we have shown previously, the preferential retention of the oxygen bubbles by the hydrophobic ZIF-8 framework leads to an enhancement in buoyancy of the micromotors that drives the motor upwards.[21] While the reaction catalyzed by GOx is oxygen consuming,[29] the reaction catalyzed by CAT is oxygen producing. This dynamic oxygen production and consumption leads to dynamic equilibrium of the buoyancy force on CAT-GOx@ZIF-8. As confirmed in Supporting Information Video 1, no sign of free bubbles or distinct bubbles was identified around the motors. In addition, oxygen consumption in bulk solution was measured with an oxygen meter in a sealed tube (Figure S9). The dissolved oxygen with different concentrations of glucose dropped to a similar level within 350 s, therefore, all the following optical and electrochemical measurements were carried out within this time scale.

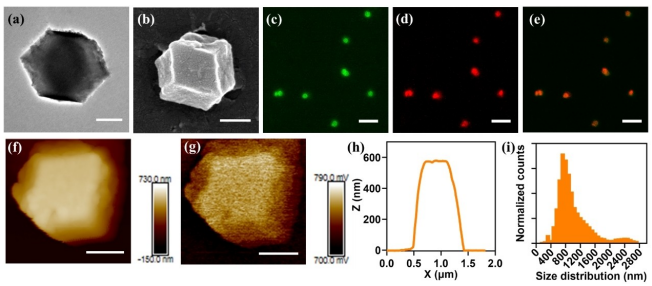

Figure 1. Characterization of CAT-GOx@ZIF-8 micromotor particles. a) TEM and b) SEM images (scale bar 300 nm). c)–e) CLSM images (scale bar 5 μm) of fluorescently labeled CAT-GOx@ZIF-8. c) CAT labeled with FITC and d) GOx labeled with AF647 in the green and red channels, respectively. e) The merged image. f) Thickness and g) surface potential distribution images from AFM (scale bar 300 nm). h) Line profile of the thickness of the particle. i) Size distribution of the particles from dynamic light scattering.

Motion Analysis of the CAT-GOx@ZIF-8 Micromotor

With the aid of an optical microscope coupled with a high-resolution camera, the motion of the micromotor travelling vertically in solution as a function of glucose concentration was recorded and analyzed (Figure 2a, Supporting Information Video S1). The mean squared displacement (MSD) with a fixed time interval Δt, representing the moving distance, is calculated according to Equation (3):

$$(\Delta x^2)|_{\Delta t} = ((x_{\Delta t} - x)^2 + (y_{\Delta t} - y)^2) \quad (3)$$

where $x_{\Delta t}$ and $y_{\Delta t}$ are the coordinates of the particle in the plane of motion after the time interval Δt. The direction of motion was evaluated by measuring the angle variation between the actual path and the horizontal line from the video, confirming their vertical motions in different glucose concentrations (Figure 2b). The dependence of the increase

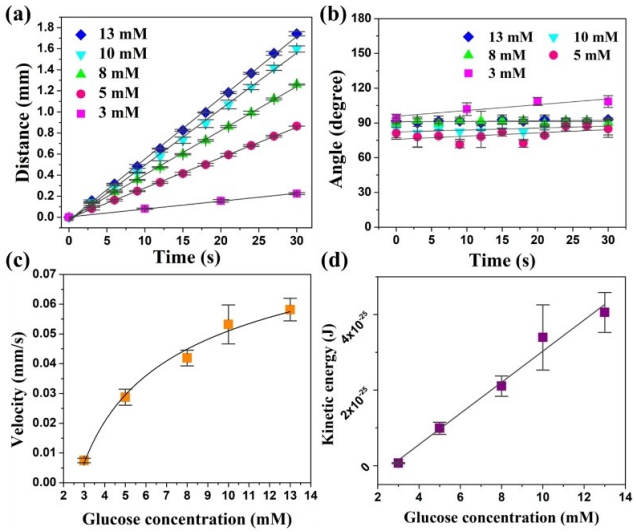

Figure 2. Motion analysis of the CAT-GOx@ZIF-8 micromotor with different glucose concentrations. a) Scatter plot of the particle ascending distance and the linear fit. b) Angle variation between the actual path and the horizontal line. c) Plot of the particle ascending velocity versus glucose concentration. d) Plot of the calculated particle kinetic energy versus glucose concentration. Error bars represent the standard deviation for three independently recorded measurements.

in ascending velocity was measured with increasing glucose concentration from 3 to 13 mM (Figure 2c). This provides a means of controlling the kinetic energy of the micromotor as it collides with the electrode which increases linearly with glucose concentration. With the estimation of the radius of the CAT-GOx@ZIF-8 motor, the kinetic energy of the motors was calculated according to Equation (4):

$$E_k = 1/2 m v^2 = 1/2 \rho V v^2 \quad (4)$$

where m is the mass, ρ is the density, V is the volume, and v is the velocity. The results indicated the positive correlation between the kinetic energy and the glucose concentration (Figure 2d, detailed calculation steps are provided in the Supporting Information).

Collision Signals with CAT-GOx@ZIF-8 Micromotors

Using a low-noise electrochemical measurement platform, the time-resolved current traces were obtained from the collision of individual micromotors at 0 mV referenced to Ag/AgCl electrode (Figure 3a). Briefly, a glassy carbon electrode of 7 μm in diameter was chosen as the working microelectrode for the impact experiment. The carbon electrode was vertically fixed on top of a vial with the surface of the electrode immersing in the bulk solution containing 2 mM NaCl, 0.1 mM $K_4Fe(CN)_6$ and 0.1 mM $K_3Fe(CN)_6$. In a typical measurement, a fixed concentration of $(4.9 \pm 1.2) \times 10^6$ mL^{-1} of CAT-GOx@ZIF-8 micromotors was applied. The micromotors were initially placed at the bottom of the working vial, and the current traces were collected soon after the signal generation was stabilized. To obtain the motor collision signals with varying kinetic energy, the glucose concentration was altered before each set of measurements.

Due to the increased buoyancy from the biocatalytic reactions, the micromotors moved vertically in the glucose solution and collided with the working electrode at the solid/liquid interface. The collisions were recorded as changes in current, which were assumed due to the disruptions of the electrical double layer (EDL) with the concomitant change in capacitive current. Relative to hydrogen peroxide-driven micromotor systems,[22] the cascade reaction-propelled motors produced oxygen bubbles with a lower velocity,[30–32] and minimized the chance for free bubbles to interfere the impact signals.

Based on the steady current of the background signals: from the blank control, without adding motors and glucose (Figure S10), as well as the systems with different concentrations of glucose (Figure S10), each current spike was ascribed to a single collision event. The current fluctuation was recorded every ≈4 μs, and the representative signals are shown in Figure 3a over a time period of 200 s. The total number of spikes was counted for each glucose concentration regardless of the shape of the signals (Figure 3b). The number of spikes was linearly correlated with the glucose concentration, indicating a correlation between the collision events and the motion intensity. The collision events increased from 40 counts at 3 mM glucose to 212 counts at 13 mM glucose in a 200 s time frame. The amplitude of each current spike was plotted as a histogram for each glucose concentration (Figure S11). Results indicated that a higher glucose concentration not only increased the maximum individual amplitude of larger peaks, but also the frequency of the smaller peaks. The residence time of each peak was collected and presented as a histogram in Figure 3c, where the most frequent residence time centered at 0.06 ms, which is 20000 times quicker compared to 1.2 s for the randomly moving micromotors.[22] The shortened residence time and the increased collision frequency may be attributed to the smaller size of the motors and the vertical moving pattern, which reduced the interaction time between the motor and the electrode surface compared to the motors moving across the electrode surface with oblique trajectories.

Possible Electrical Signal Generation Mechanism with CAT-GOx@ZIF-8 Micromotors

Due to the fact that ZIF-8 particles are not electroactive,[33,34] as evident from the cyclic voltammograms of the CAT-GOx@ZIF-8 in Figure S12–S14, the micromotor is expected to be non-electrocatalytic and redox-inactive at 0 mV vs Ag/AgCl reference electrode. On the basis of the steady current signals from the control groups, the spikes were associated with the motor-electrode collision events. Previously, micromotor collision experiments with uniform downward spikes were attributed to the blocking impact, where the electric current was hindered by the blocking of

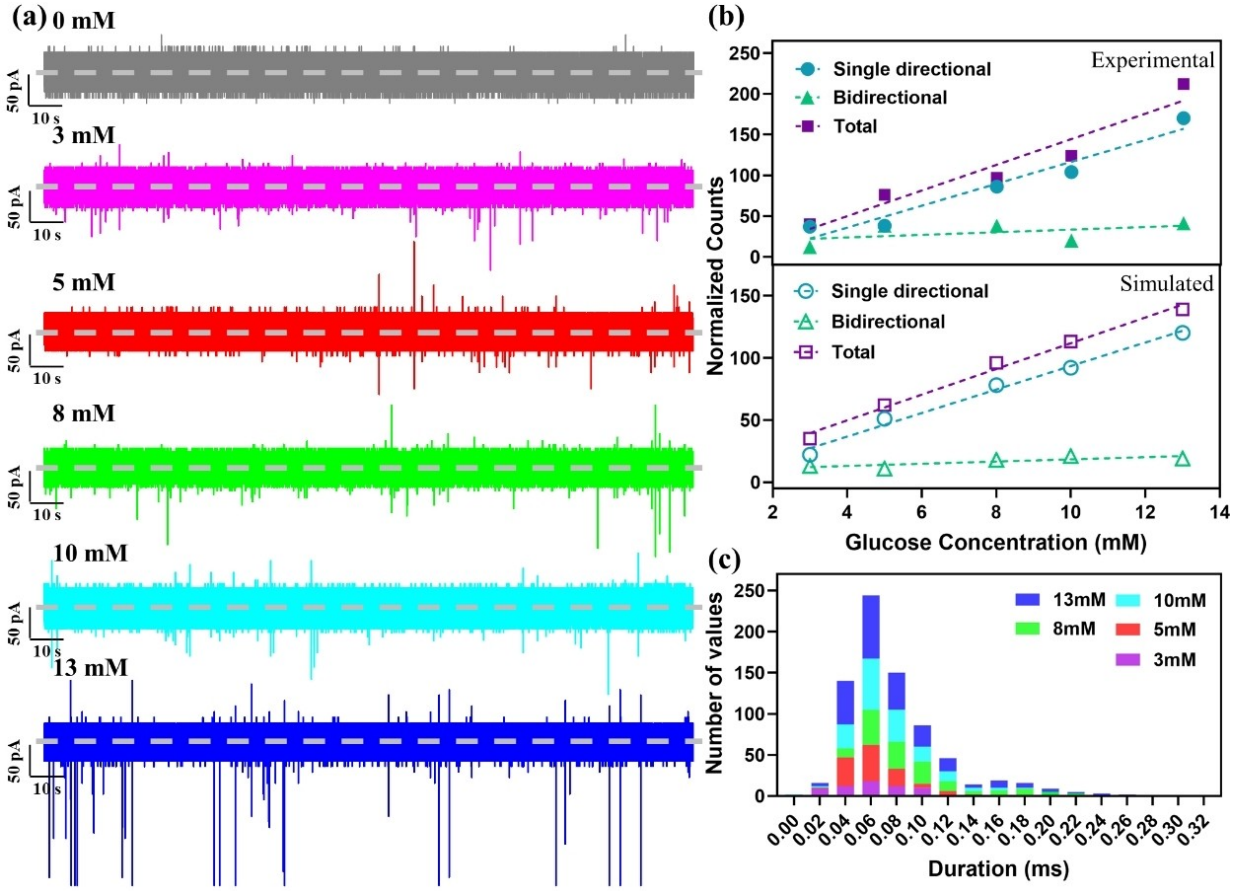

Figure 3. Collision signals with CAT-GOx@ZIF-8 micromotors at 7 μm carbon microelectrode. a) Time-dependent current recordings with increased glucose concentration from 3 to 13 mM. b) Experimental and simulated spike counts for single directional spikes and bidirectional spikes with increased glucose concentration. c) Histogram of the residence time of spikes with increased glucose concentration from 3 to 13 mM.

electrode surface from both micromotors and the emitted bubbles.[22] However, the origin of current signals with bidirectional spikes under fixed experimental condition has seldomly been discussed.

Among a range of electrochemically inactive particle collision events, the direction of the spikes in capacitive impacts was altered with different potentials that are higher/lower than the potential of zero charge (PZC),[35] where the electrical double layer (EDL) was perturbed through a charging-discharging process. Due to the perturbation of the charge distribution at the electrical double layer of the working electrode surface, the capacitive events gave rise to spike-shaped signals at mercury electrodes and solid microelectrodes.[36–38] The approaching-and-departing process of the impacting particles resulted in an electron flow at the electrode side via transient exclusion of ions from the EDL.

Inspired by these stochastic collision experiments, our micromotors with vertical motion are expected to have repeated approaching-and-departing processes, which are most likely to cause the current signals with initiative charging/discharging processes. Under the applied conditions, the PZC of the 7 μm carbon microelectrode was measured to be −0.29 V vs. Ag/AgCl (Figure S15). Taking the current signals from the CAT-GOx@ZIF-8 micromotors with 10 mM glucose at a potential of 0 mV vs. Ag/AgCl as an example (Figure 4a), four representative patterns, singular downward (Figure 4b), singular upward (Figure 4c), bidirectional downward-upward (Figure 4d) and bidirectional upward-downward (Figure 4e) signals, were obtained in a single impact experiment. The respective singular downward and upward signals were believed to be associated with the approaching and departing process of the motors from the electrode. When the motors gained increased buoyancy and floated up, the approaching of the motors to the electrode resulted in singular downward spikes, which had similar effect as the adhesive particles with blocking mechanism. The floated motors resting at the interface may be disrupted by the subsequently approached motors or the inner oxygen consumption induced buoyancy decrease. When the motors departed from the electrode, the reorganization of the ions in the EDL resulted in upward spikes.

The number of the singular spikes was counted to be positively correlated with the glucose concentration (Figure 3b). Unlike the collisions based on Brownian motion, the dynamic cascade reaction of oxygen production and consumption leads to dynamic equilibrium between buoy-

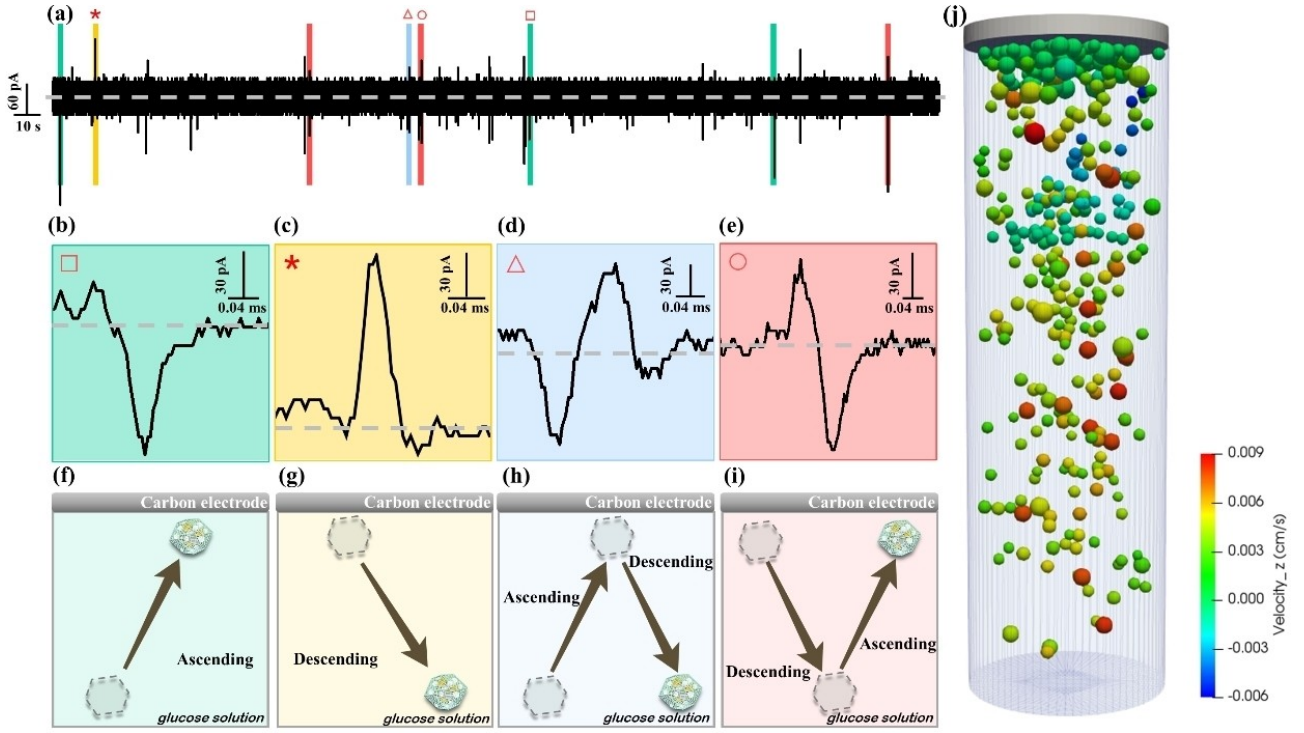

Figure 4. Collision signals with CAT-GOx@ZIF-8 micromotors at 7 μm carbon microelectrode. a) Current-time recording of individual micromotor collisions at 0 mV vs. Ag/AgCl in electrolyte solution containing 10 mM glucose. b)–e) Close-ups of the representative current traces, corresponding to the spikes in (a). f)–i) Simulated illustration of the representative motion patterns. j) The snapshots of motion state from simulated video with 13 mM glucose in electrolyte.

ancy force and the overall force direction exerted on the motors. The floated motors resting at the interface may be collided by the subsequently approached micromotors, which could also disturb the force balance. The dynamic force balance of the motors resulted in the repeated approaching-and-departing processes and complex collision patterns. The bidirectional downward-upward spikes were ascribed to the immediate departing of the motor once it reached the electrode, which may be resulted from the consumption of oxygen bubbles, the bounce from the electrode, or the disturbance from other floating micromotors. Similarly, the departing motors could be pushed back by the subsequent floating ones, which resulted in inverse bidirectional motion and upward-downward spikes. With the dynamic chemical reactions, the dropped motors with reproduced bubbles could also float again to produce the bidirectional upward-downward spikes. The number of the bidirectional spikes was also dependent on the concentration of glucose (Figure 3b).

Particle-Scale Numerical Simulation of Micromotor Motion

To verify the motion patterns of the motors, a particle-scale computational fluid dynamics (CFD) simulation was applied to reproduce the solid–liquid interaction and the particles impact on the electrode (Figure 4j, Supporting Information Video S2). The fluid flow was modelled by the finite volume method (FVM) with the Navier-Stokes equations, the solid phase motion was modelled by discrete element method (DEM) with Newton's second law of motion, and the interaction between solid and liquid phases was realized by their momentum transfer using the drag force.[39]

To simulate the experimental conditions, the numerical modelling was carried out under a narrow cylinder column with the electrode on the top, and the particles with size distribution were randomly generated in the particle generation region (Figure S16–S20). The liquid was set as five different glucose concentrations and the motion of the particles was governed by gravity, drag force, buoyance force, contact force and van der Waals force (Figure S21). The localized, dynamic oxygen consumption and production from the catalytic cascade reaction changed the buoyance forces of the particles, leading to the occurrence of different motion patterns. The motion patterns were explained from the force view.

Two patterns were confirmed after particle impacting on the electrode: particles attaching to the electrode (pattern #1, Figure 4f), and particles impacting on the electrode and then moving downwards (pattern #3, Figure 4h). The consumption of glucose led to the increase of buoyancy force, and when the buoyance force could still outweigh the downward forces, the particle will remain attached on the electrode. Conversely, the particle would move downwards after impacting on the electrode due to the downward net force. The number of particles in pattern #1 was significantly

larger than that in pattern #3, therefore a particle layer could be formed around the electrode. Subsequently, the later ascending particles would impact on the particle layer and disrupt the force balance of the already collided particles, as evidenced by the stationary particles descending from the top region over a period of time (pattern #2, Figure 4g). The signal pattern #2 could also be induced by decreased buoyancy force with net oxygen consumption. Meanwhile, the descending particles could regain upward force with the generation of oxygen bubbles and hence the descending velocity gradually slowed down, while a small proportion of motors would ascend again once they regain enough buoyancy from the continuous biocatalytic cascades (pattern #4, Figure 4i). Finally, the statistic from the simulation was plotted in Figure 3b, and the results closely resembled the actual collision events, which verified the proposed signal generation mechanism from the experimental observation.

Conclusion

In this work, we explored the collision signals of the CAT-GOx@ZIF-8 micromotors with controllable vertical motion and discussed the possible signal generation mechanism based on capacitive impact theory. With coupled biocatalytic cascade reaction converting biocompatible fuel glucose to oxygen microbubbles, the system endowed the motors with heterogeneous motion patterns, which created possibilities of generating various collision signals compared to the previous electrochemically inactive particles. With the aid of particle-scale numerical simulation using CFD-DEM model, four distinctive electrical impact patterns corresponding to the motion patterns of motors were discussed and verified, and the underlying mechanisms were revealed by force analysis. With the proposed micromotor system, this work offers a chance of exploring the real-time interaction between non-electrocatalytic and redox-inactive particles and electrical signal generation, providing a new dimension to carry out collision experiments.

Acknowledgements

This work was supported by the Australia National Health and Medical Research Council (NHMRC, GNT1163786), the Australian Research Council (ARC, DP210100422), the National Breast Cancer Foundation, Australia (IIRS-22-104), and the Scientia program at UNSW. The authors acknowledge the facilities and the scientific and technical assistance of Microscopy Australia at the Electron Microscope Unit (EMU) within the Mark Wainwright Analytical Centre (MWAC) at UNSW Sydney. The authors also acknowledge the Surface Analysis Laboratory and Spectroscopy laboratory and Molecular Surface Interaction Network Laboratory at UNSW for materials characterizations. Z.G. acknowledges the Australian Government Research Training Program Scholarship. Open access publishing facilitated by University of New South Wales, as part of the Wiley - University of New South Wales agreement via the Council of Australian University Librarians. Open Access publishing facilitated by University of New South Wales, as part of the Wiley - University of New South Wales agreement via the Council of Australian University Librarians.

Conflict of Interest

The authors declare no conflict of interest.

Data Availability Statement

The data that support the findings of this study are available on request from the corresponding author. The data are not publicly available due to privacy or ethical restrictions.

Keywords: Biocatalysis · Electrochemistry · Metal–Organic Frameworks · Micromotors · Particle Impact

[1] J. J. Gooding, *Angew. Chem. Int. Ed.* **2016**, *55*, 12956–12958; *Angew. Chem.* **2016**, *128*, 13148–13150.
[2] L. A. Baker, *J. Am. Chem. Soc.* **2018**, *140*, 15549–15559.
[3] Z. Sun, M. E. Hafez, W. Ma, Y. T. Long, *Sci. China Chem.* **2019**, *62*, 1588–1600.
[4] F. T. Patrice, K. Qiu, Y. L. Ying, Y. T. Long, *Annu. Rev. Anal. Chem.* **2019**, *12*, 347–370.
[5] L. K. Allerston, N. V. Rees, *Curr. Opin. Electrochem.* **2018**, *10*, 31–36.
[6] H. Ma, J. F. Chen, H. F. Wang, P. J. Hu, W. Ma, Y. T. Long, *Nat. Commun.* **2020**, *11*, 2307.
[7] P. Pandey, J. Garcia, J. Guo, X. Wang, D. Yang, J. He, *Nanotechnology* **2020**, *31*, 015503.
[8] S. K. Mun, S. Lee, D. Y. Kim, S. J. Kwon, *Chem. Asian J.* **2017**, *12*, 2434–2440.
[9] P. A. Defnet, T. J. Anderson, B. Zhang, *Curr. Opin. Electrochem.* **2020**, *22*, 129–135.
[10] T. H. T. Nguyen, J. Lee, H. Y. Kim, K. M. Nam, B. K. Kim, *Biosens. Bioelectron.* **2020**, *151*, 111999.
[11] K. Chuah, Y. Wu, S. R. C. Vivekchand, K. Gaus, P. J. Reece, A. P. Micolich, J. J. Gooding, *Nat. Commun.* **2019**, *10*, 2109.
[12] J. Wang, R. Dong, H. Wu, Y. Cai, B. Ren, *Nano-Micro Lett.* **2019**, *12*, 11.
[13] F. Peng, Y. Tu, D. A. Wilson, *Chem. Soc. Rev.* **2017**, *46*, 5289–5310.
[14] J. Parmar, D. Vilela, K. Villa, J. Wang, S. Sanchez, *J. Am. Chem. Soc.* **2018**, *140*, 9317–9331.
[15] Y. Tu, F. Peng, D. A. Wilson, *Adv. Mater.* **2017**, *29*.
[16] C. Zhou, P. Zhu, Y. Tian, M. Xu, L. Wang, *ACS Nano* **2019**, *13*, 6319–6329.
[17] H. Su, C. A. Hurd Price, L. Jing, Q. Tian, J. Liu, K. Qian, *Mater. Today Bio* **2019**, *4*, 100033.
[18] Z. Guo, T. Wang, A. Rawal, J. Hou, Z. Cao, H. Zhang, J. Xu, Z. Gu, V. Chen, K. Liang, *Mater. Today* **2019**, *28*, 10–16.
[19] T. Patino, A. Porchetta, A. Jannasch, A. Llado, T. Stumpp, E. Schaffer, F. Ricci, S. Sanchez, *Nano Lett.* **2019**, *19*, 3440–3447.
[20] Y. Peng, H. Huang, Y. Zhang, C. Kang, S. Chen, L. Song, D. Liu, C. Zhong, *Nat. Commun.* **2018**, *9*, 187.
[21] Z. Guo, J. Liu, Y. Li, J. A. McDonald, M. Y. Bin Zulkifli, S. J. Khan, L. Xie, Z. Gu, B. Kong, K. Liang, *Chem. Commun.* **2020**, *56*, 14837–14840.
[22] J. G. S. Moo, M. Pumera, *ACS Sens.* **2016**, *1*, 949–957.

[23] C. Kloss, C. Goniva, A. Hager, S. Amberger, S. Pirker, *Prog. Comput. Fluid Dyn.* **2012**, *12*, 140–152.
[24] K. Liang, J. J. Richardson, J. Cui, F. Caruso, C. J. Doonan, P. Falcaro, *Adv. Mater.* **2016**, *28*, 7910–7914.
[25] K. Liang, C. J. Coghlan, S. G. Bell, C. Doonan, P. Falcaro, *Chem. Commun.* **2016**, *52*, 473–476.
[26] K. Liang, R. Wang, M. Boutter, C. M. Doherty, X. Mulet, J. J. Richardson, *Chem. Commun.* **2017**, *53*, 1249–1252.
[27] K. Liang, R. Ricco, C. M. Doherty, M. J. Styles, S. Bell, N. Kirby, S. Mudie, D. Haylock, A. J. Hill, C. J. Doonan, P. Falcaro, *Nat. Commun.* **2015**, *6*, 7240.
[28] W. Melitz, J. Shen, S. Lee, J. S. Lee, A. C. Kummel, R. Droopad, E. T. Yu, *J. Appl. Phys.* **2010**, *108*, 023711.
[29] J. C. Bouin, M. T. Atallah, H. O. Hultin, *Methods in Enzymology, Vol. 44*, Academic Press, New York, **1976**, pp. 478–488.
[30] E. M. Kutorglo, R. Elashnikov, S. Rimpelova, P. Ulbrich, J. Rihova Ambrozova, V. Svorcik, O. Lyutakov, *ACS Appl. Mater. Interfaces* **2021**, *13*, 16173–16181.
[31] L. K. Abdelmohsen, M. Nijemeisland, G. M. Pawar, G. J. Janssen, R. J. Nolte, J. C. van Hest, D. A. Wilson, *ACS Nano* **2016**, *10*, 2652–2660.
[32] M. Liu, L. Chen, Z. Zhao, M. Liu, T. Zhao, Y. Ma, Q. Zhou, Y. S. Ibrahim, A. A. Elzatahry, X. Li, D. Zhao, *J. Am. Chem. Soc.* **2022**, *144*, 3892–3901.
[33] S. Payra, S. Challagulla, C. Chakraborty, S. Roy, *J. Electroanal. Chem.* **2019**, *853*, 113545.
[34] Y. Wang, P. Hou, Z. Wang, P. Kang, *ChemPhysChem* **2017**, *18*, 3142–3147.
[35] E. Laborda, A. Molina, C. Batchelor-McAuley, R. G. Compton, *ChemElectroChem* **2018**, *5*, 410–417.
[36] D. Hellberg, F. Scholz, F. Schauer, W. Weitschies, *Electrochem. Commun.* **2002**, *4*, 305–309.
[37] F. Scholz, D. Hellberg, F. Harnisch, A. Hummel, U. Hasse, *Electrochem. Commun.* **2004**, *6*, 929–933.
[38] J. Poon, C. Batchelor-McAuley, K. Tschulik, R. G. Compton, *Chem. Sci.* **2015**, *6*, 2869–2876.
[39] Z. Xie, S. Wang, Y. Shen, *Chem. Eng. Sci.* **2021**, *231*, 116261.

Manuscript received: July 4, 2022
Accepted manuscript online: August 10, 2022
Version of record online: August 25, 2022